

Supporting Information

Bithiophene Dicarboxylate as Efficient Organic Anode

Material for Sodium-Ion Batteries

Contents

1. General Methods

2. Experimental Section

3. Spectra

Figure S1. ^1H NMR spectrum of PTDA in CDCl_3 .

Figure S2. ^1H NMR spectrum of PTDC in d-DMSO.

Figure S3. ^1H NMR spectrum of PT in D_2O .

Figure S4. ^{13}C NMR spectrum of PT in D_2O .

Figure S5. ESI-MS of PT.

Figure S6. ^1H NMR spectrum of BT in D_2O .

Figure S7. ^{13}C NMR spectrum of BT in D_2O .

Figure S8. ESI-MS of BT.

Figure S9. FESEM image of (a) BT and (b) PT.

Figure S10. FTIR spectra of PTDC and PT

Figure S11. UV-vis spectra of solubility experiments with (a) BT and (b) PT electrode sheet immersed in 1.0 M NaCF_3SO_3 (in TETRAGLYME=100 Vol%).

Figure S12. (a) Cycling performance and coulombic efficiency of the PT electrode at 0.2C. (b) Long-term cyclability of PT at a current density of 2.0C. (c) Rate performance of PT at different current densities from 0.2C to 2.0C.

Figure S13. (a) Cycling performance and coulombic efficiency of the BP electrode at 0.2C. (b) Long-term cyclability of BP at a current density of 2.0C. (c) Rate performance of BP at different current densities from 0.2C to 2.0C.

Figure S14. Galvanostatic discharge/charge profiles of (a) BT, (b) PT and (c) BP at a current density

of 0.2C.

Figure S15. (a) CV curves of BT at 0.2 mV s⁻¹. (b) Nyquist plots of BT electrodes charged to 2.5 V after different cycles. (c) GITT curves and (d) the calculated Na-ion diffusion coefficients for BT electrode.

Figure S16. (a) CV curves of PT at 0.2 mV s⁻¹. (b) Nyquist plots of PT electrodes charged to 2.5 V after different cycles. (c) GITT curves and (d) the calculated Na-ion diffusion coefficients for PT electrode.

Figure S17. The equivalent circuits of EIS data for BT and PT in Na-ion batteries. R_s: electrolyte resistance, R_{ct}: charge transfer resistance, R_f: contact resistance of SEI films, CPE: constant phase element, and W_o: Warburg impedance. The simulated impedance parameters were determined by fitting the original EIS spectra using Z View software (inset).

Figure S18. The calculated MESP distribution and the potential energy (ΔE) of PT with different numbers of Na⁺.

Figure S19. The calculated MESP distribution and the potential energy (ΔE) of BP with different numbers of Na⁺.

Figure S20. Ex-situ S 2p XPS spectra of the BT electrode in various states: pristine, discharged to 0.1 V and recharged to 2.5 V.

Figure S21. (a) Schematic diagram of the full battery during charging; (b) Cycle performance of full battery at 100 mA g⁻¹

Table S1. Performances comparison between our anode and some reported organic anode materials for SIBs.

Table S2. The thermal decomposition temperature comparison between our anode and some reported organic anode materials for SIBs.

Table S3. Resistances of BT and PT in Na-ion batteries obtained from equivalent circuit fitting of impedance data.

Table S4. Calculated LUMO and HOMO energies and distributions of BT, BT-Na and BT-2Na.

Table S5. Calculated LUMO and HOMO energies and distributions of PT, PT-Na and PT-2Na.

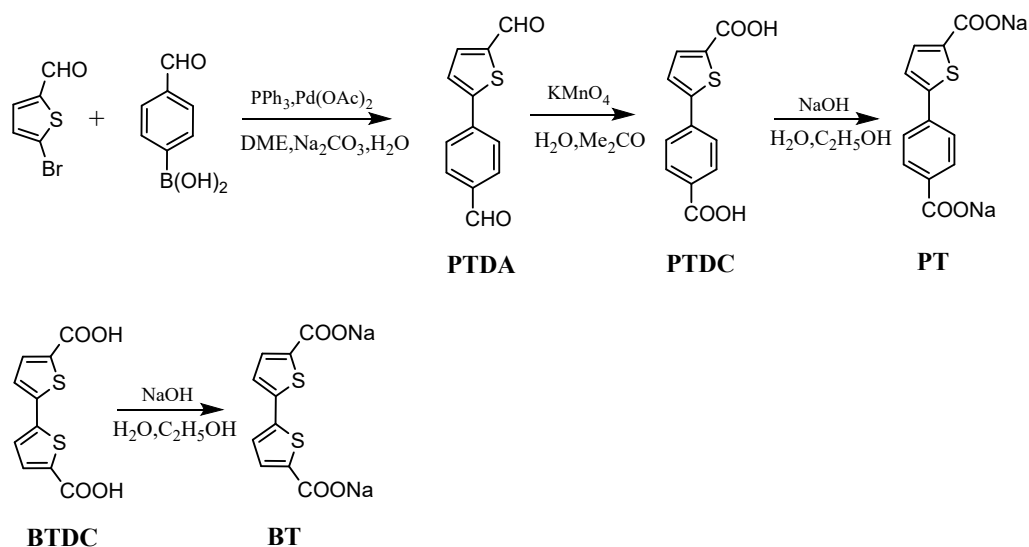
Table S6. Calculated LUMO and HOMO energies and distributions of BP, BP -Na and BP -2Na.

1. General Methods

Unless otherwise stated, all starting materials were purchased from commercial suppliers (Sigma Aldrich, and the Energy Chemical) and used without further purification. 5-bromo-2-thiophenecarboxaldehyde (Adamas), 4-formylphenylboronic acid (Adamas), [2,2'-bithiophene]-5,5'-dicarboxylic acid (Adamas), [1,1'-biphenyl]-4,4'-dicarboxylic acid (Adamas), NaOH (Greagent, AR), Ethanol (Greagent, AR), N-Methyl-2-pyrrolidinone (Greagent, >99.0%) were purchased and used without further purification.

2. Experimental Section

Materials Synthetic:



Scheme S1 the synthetic route of compounds **PT** and **BT**.

Synthesis of sodium 5-(4-carboxylatophenyl) thiophene-2-carboxylate (PT):

Step1: To a dry glass flask purged with argon were added $\text{Pd}(\text{OAc})_2$ (58 mg, 0.26 mmol), PPh_3 (280 mg, 1 mmol) and dry DME (40 mL). The resultant solution was stirred at room temperature for 10 min, and 5-bromo-2-thiophenecarboxaldehyde (0.6 mL, 52 mmol) and Na_2CO_3 (aq) (2 M, 6 mL, 12 mmol) were added. After 5 min a 4-formylphenylboronic acid (0.98 g, 6.6 mmol) was added and reaction mixture was purged with argon and refluxed for 3 h under argon. The solution was cooled to room temperature and filtered through a pad of Celite, washed with CH_2Cl_2 and dried with anhydrous Na_2SO_4 . The organic solvent was removed under reduced pressure and the crude product was purified by dry-flash chromatography (SiO_2 : hexane/EtOAc = 7:3) to afford 5-(4-formylphenyl)thiophene-2-carbaldehyde (PTDA) (1.08 g, 96%) as a pale-yellow amorphous powder. ^1H NMR (600 MHz, CDCl_3): δ 10.05 (s, 1H), 9.94 (s, 1H), 7.95 (d, $J = 8.2$ Hz, 2H), 7.84 (d, $J = 8.2$ Hz, 2H), 7.79 (d, $J = 3.9$ Hz, 1H), 7.54 (d, $J = 3.9$ Hz, 1H).

Step2: Add excess potassium permanganate (3.66 mg, 23.15 mmol) to PTDA (1.0 g, 4.63 mmol), add water (15 mL) and acetone (60 mL) solvent, and react at 50°C for one day until the color of the solution changes from purplish red to brown. After the reaction, acetone was removed from the reaction mixture, and then water (50 mL) was added to the residue, the mixture was filtered and acidified by slowly adding concentrated hydrochloric acid to the filtrate, white precipitation was obtained by filtration and vacuum drying to obtain the product. The crude product was recrystallized from DCM and methanol to obtain the final product 5-(4-carboxyphenyl) thiophene-2-carboxylic acid (PTDC) (0.96 g, 85%). ¹H NMR (600 MHz, DMSO) δ 13.20 (s, 2H), 8.01 (d, *J* = 8.2 Hz, 2H), 7.88 (d, *J* = 8.3 Hz, 2H), 7.74 (dd, *J* = 28.8, 3.8 Hz, 2H).

Step3: To a stirred aqueous suspension (10.0 mL) of PTDC (1.0 g, 4.1 mmol), an aqueous solution (5.0 mL) of NaOH (0.5 g, 12.5 mmol) was added at room temperature. After the completion of the reaction, the solution was filtered, and ethanol (30.0 mL) was added to the filtrate, resulting in yellowish precipitates (PT). The yellowish precipitate obtained was filtered, washed with ethanol, and dried in air. Yield: 0.96 g (81.3%). ¹H NMR (600 MHz, D₂O) δ 7.89 (d, *J* = 7.8 Hz, 2H), 7.78 (d, *J* = 7.3 Hz, 2H), 7.55 (s, 1H), 7.49 (s, 1H). ¹³C NMR (151 MHz, D₂O) δ 175.06 (s), 169.84(s), 147.19 (s), 140.85 (s), 136.00 (s), 135.85 (s), 132.01 (s), 129.67 (s), 125.50 (s), 124.82 (s).

Synthesis of sodium [2,2'-bithiophene]-5,5'-dicarboxylate (BT):

To a stirred aqueous suspension (10.0 mL) of [2,2'-bithiophene]-5,5'-dicarboxylic acid (BTDC (1.0 g, 3.9 mmol)), an aqueous solution (5.0 mL) of NaOH (0.5 g, 12.5 mmol) was added at room temperature. After the completion of the reaction, the solution was filtered, and ethanol (30.0 mL) was added to the filtrate, resulting in yellow precipitates (BT). The yellow precipitate obtained was filtered, washed with ethanol, and dried in air. Yield: 0.98 g (83%). ¹H NMR (600 MHz, D₂O) δ

7.47 (d, $J = 7.8$ Hz, 2H), 7.30 (d, $J = 9.2$ Hz, 2H). ^{13}C NMR (151 MHz, D_2O) δ 169.60 (s), 140.66(s), 140.45 (s), 131.76 (s), 125.16 (s).

Material characterizations: The nuclear magnetic resonance (NMR) spectra were obtained from a BRUKER AVANCE III 600 MHz NMR Instrument (in CDCl_3). Data for ^1H NMR are recorded as follows: chemical shift (ppm), multiplicity (s, singlet; d, doublet; t, triplet; q, quarter; m, multiple), coupling constant (Hz), integration. Data for ^{13}C NMR are reported in terms of chemical shift (δ , ppm). JSM-7800F field emission scanning electron microscope was used to characterize morphology. The crystal structures were analyzed using MAXima-X XRD-7000. The Fourier transform infrared spectrometer (FT-IR) was recorded using KBr pellets on a Thermo Nicolet 6700 with the wavenumber range of $400\text{-}4000\text{ cm}^{-1}$. Thermal gravimetric analysis (TGA, Q50) was detected in nitrogen (N_2) conditions.

Electrochemical tests: For the half cell, the working electrodes were prepared by casting the slurry onto a clean Al foil, where the slurry contained the active materials (60 wt%), carbon black (Super P, 30 wt%), and poly (vinylidene fluoride) binder (PVDF, 10 wt%). Then, the collector was dried overnight at $60\text{ }^\circ\text{C}$. The separator was Whatman glass fiber. The samples of electrochemically active materials were evaluated in 2032-type coin cells with a Na disk as the counter electrode and $1.0\text{M NaCF}_3\text{SO}_3$ (in TETRAGLYME=100 Vol%, Duoduo chemical reagent Co., LTD, Suzhou). The average loading of active materials was $0.8\text{-}1.3\text{ mg cm}^{-2}$. All battery assembly and disassembly are performed in a dry Ar-filled glove box ($\text{H}_2\text{O} < 0.1\text{ ppm}$, $\text{O}_2 < 0.1\text{ ppm}$ Mikrouna).

The galvanostatic cycling test was carried on a CT-4008T instrument (Shen Zhen NEWARE electronic Co.). Cyclic voltammograms (CVs) were tested on a CHI instrument electrochemical workstation (Corrtest CS310H) at a scan rate of 0.1 mV s^{-1} between 0.1 and 2.5 V (vs Na^+/Na). The electrochemical impedance spectroscopy (EIS) test was measured by a CHI instrument electrochemical workstation in the frequency range of 10^{-2} - 10^5 Hz at the amplitude of 5 mV. All the tests were performed at room temperature (25°C).

Ex-situ FTIR and ex-situ XPS spectroscopy: In an argon-filled glove box, the electrode sheets were taken out of the batteries at different charging and discharging states, and then washed with DME to remove the remaining electrolyte. It was then vacuum dried at 60°C for 6 hours. Then the marked electrodes were stored in an argon atmosphere. The samples were quickly taken out of the argon-filled box for each test. And these samples were exposed to air when conducting ex-situ measurements. For ex-situ FTIR tests, the products at different charge and discharge states were tested using the ATR pattern. For ex-situ XPS tests, the sample was prepared in a stream of Ar-flow, and then the XPS measurement was conducted.

Computational details : Geometric structures and electronic properties of the investigated systems were fully optimized using B3LYP at 6-31G(d,p) levels. The energies of all of the obtained geometries are ensured to be the lowest because the optimized structures do not exhibit imaginary frequency. All calculations were carried out by the Gaussian 09 program.

XPS fitting method: The CasaXPS software was used to perform peak fitting of the

original data, and the Origin2018 software was used to plot the exported data. In the process of fitting, the FWHM is limited to be between 1 and 2 eV.

GITT test:

The Na⁺ diffusion coefficient (D_{Na^+}) was calculated by the galvanostatic intermittent titration technique measurement (GITT) method according to the following equation :

$$D_{Na^+} = \frac{4(n_m V_m)}{\pi S} \left(\frac{\Delta E_s}{\tau(dE_t/d\sqrt{\tau})} \right)^2 = \frac{4(n_m V_m)}{\pi \tau S} \left(\frac{\Delta E_s}{\Delta E_t} \right)^2 \dots\dots (S1)$$

where τ is the pulse time, n_m is the mole number, V_m is the molar volume, S is the electrode-electrolyte interface area, ΔE_s is the voltage difference between the steady-state and the initial state of every step, and ΔE_t is the change of total voltage during a pulse step excluding the IR drop.

3.Spectra:

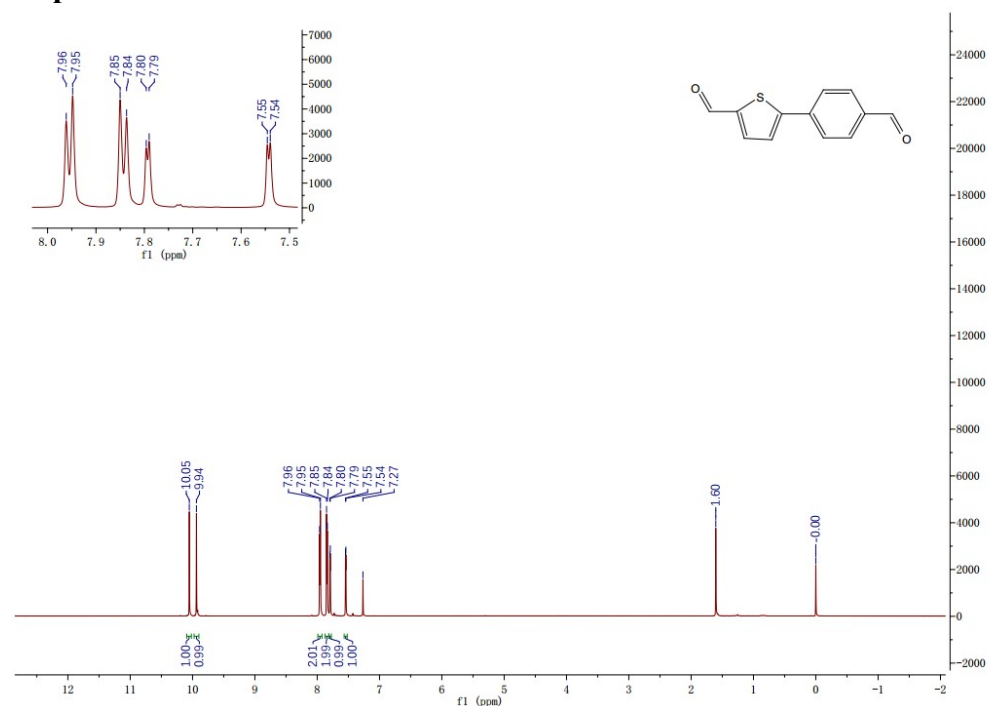


Figure S1. ^1H NMR spectrum of PTDA in CDCl_3 .

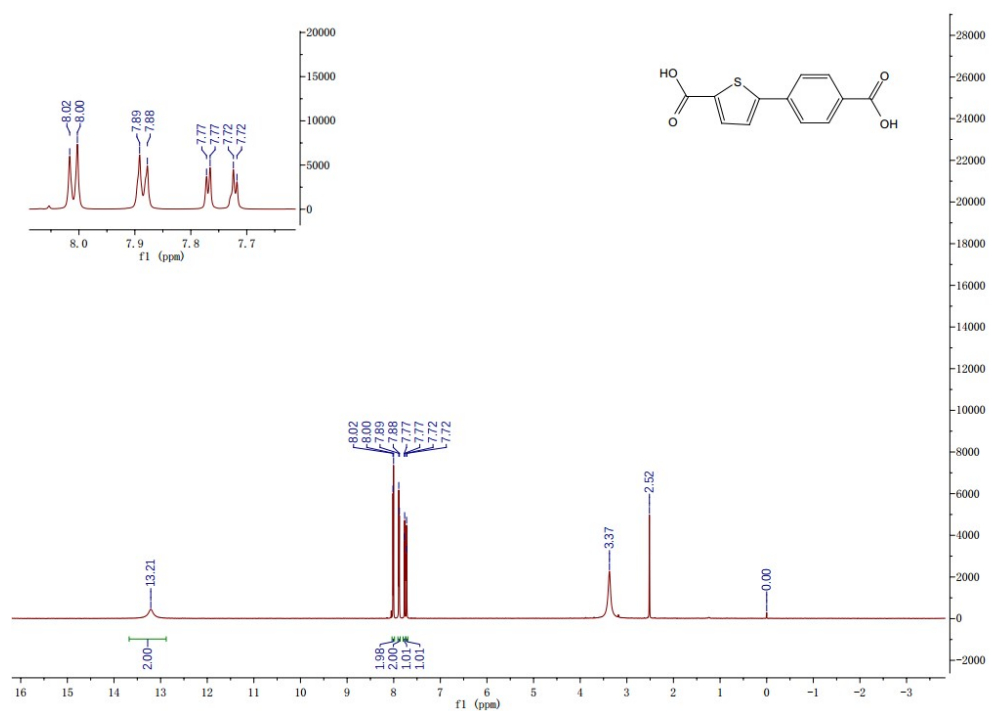


Figure S2. ^1H NMR spectrum of PTDC in $d\text{-DMSO}$.

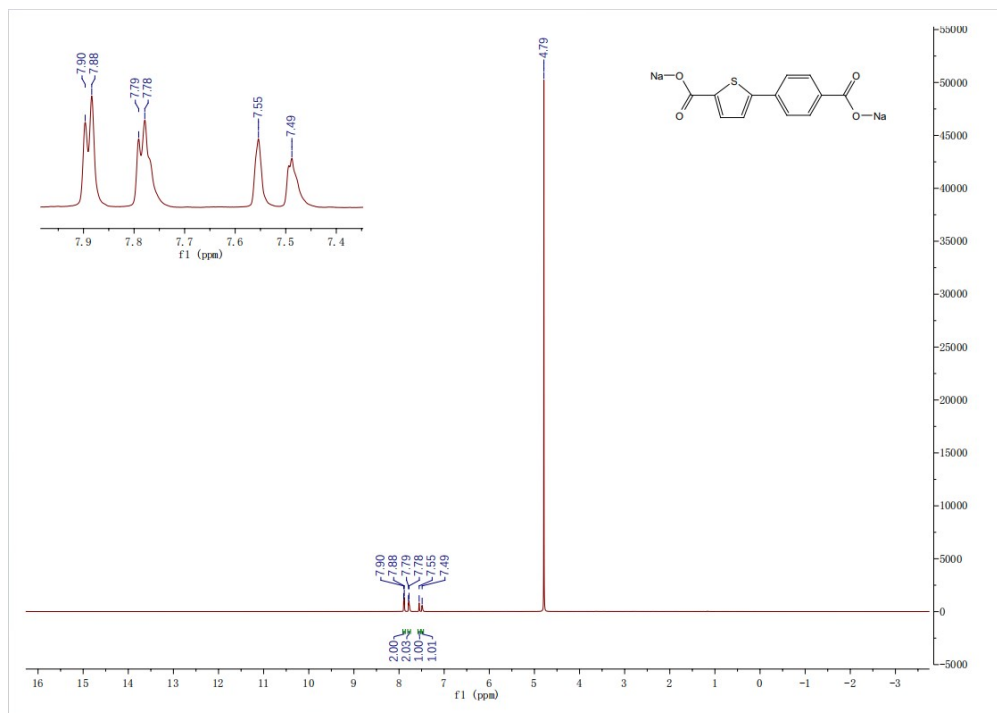


Figure S3. ¹H NMR spectrum of PT in D₂O.

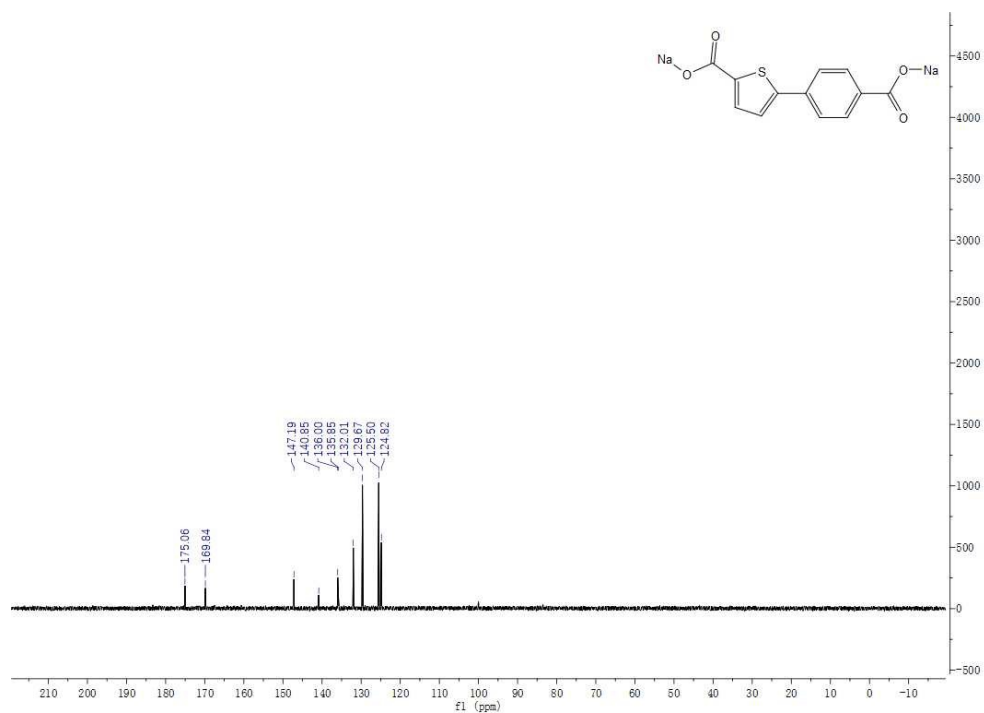


Figure S4. ¹³C NMR spectrum of PT in D₂O.

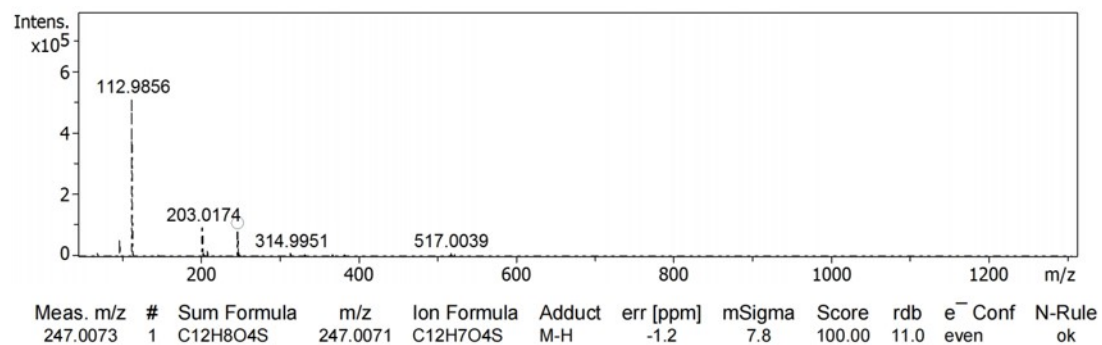


Figure S5. ESI-MS of PT.

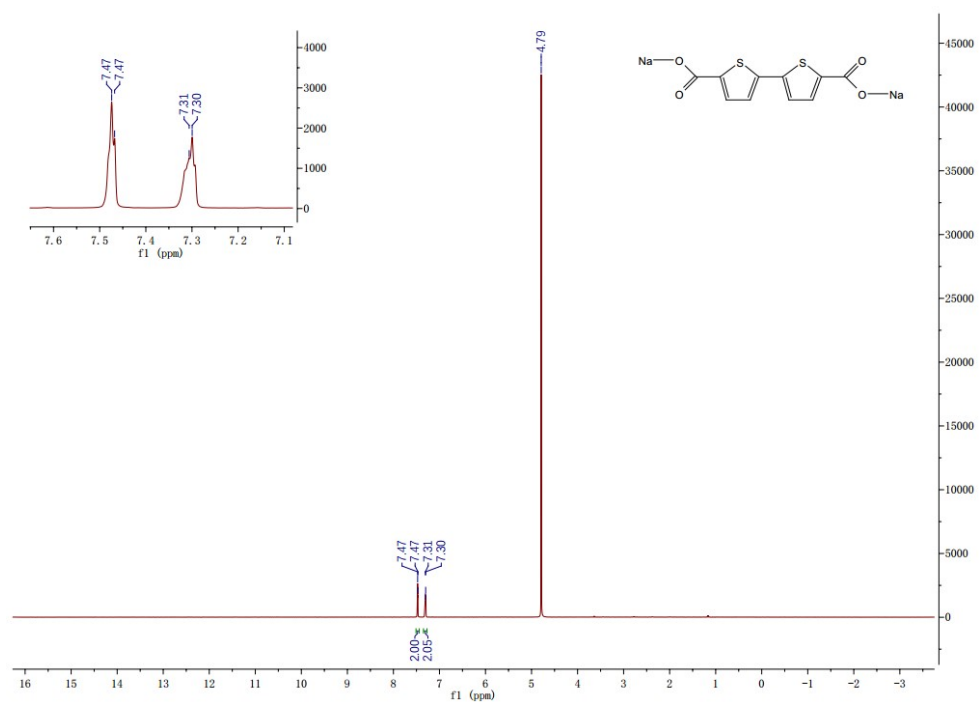


Figure S6. ¹H NMR spectrum of BT in D₂O.

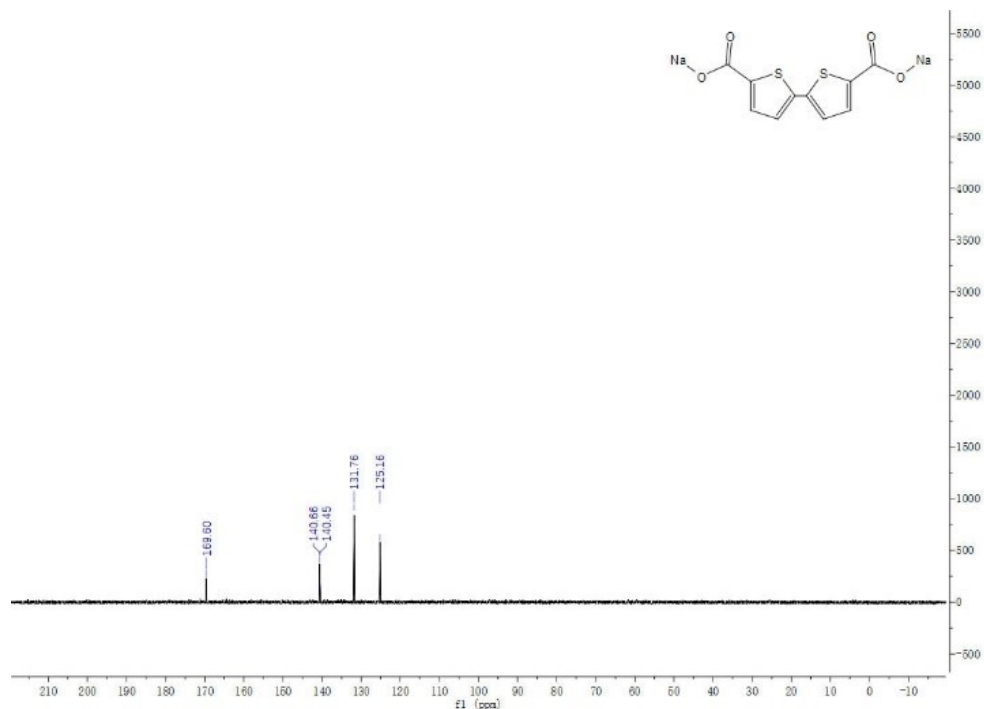


Figure S7. ^{13}C NMR spectrum of BT in D_2O .

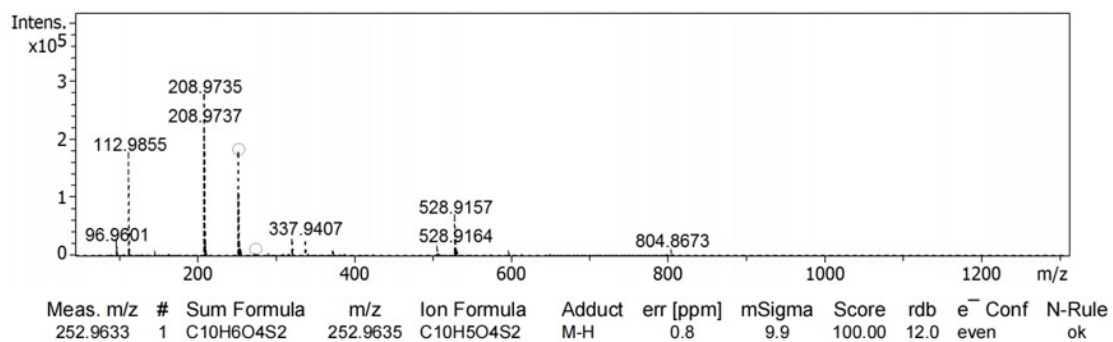


Figure S8. ESI-MS of BT.

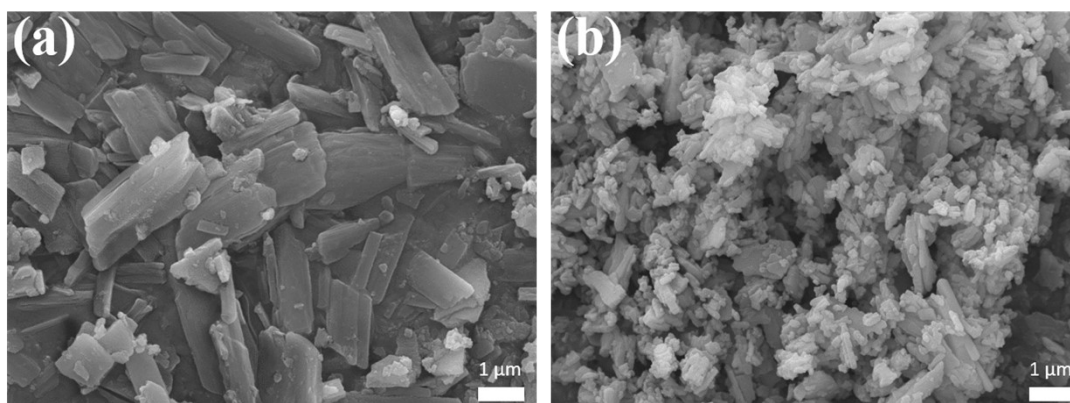


Figure S9. FESEM image of (a) BT and (b) PT.

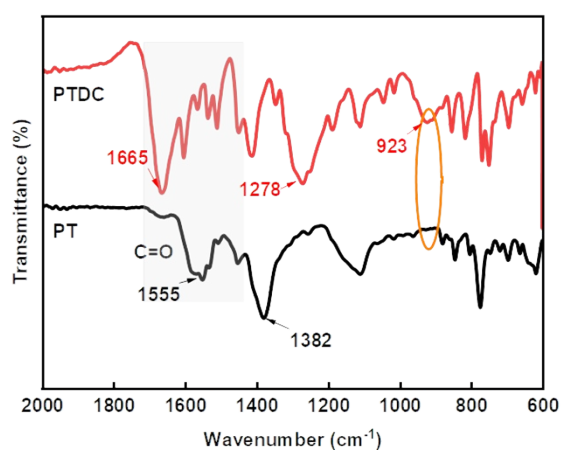


Figure S10. FTIR spectra of PTDC and PT

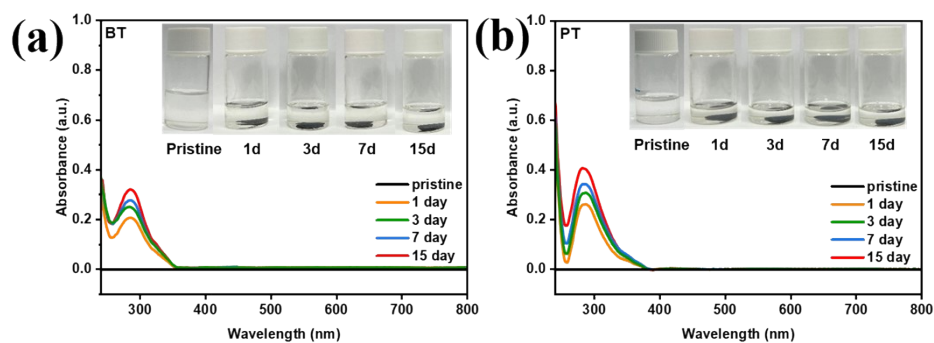


Figure S11. UV-vis spectra of solubility experiments with (a)BT and (b)PT electrode sheet immersed in 1.0 M NaCF_3SO_3 (in TETRAGLYME=100 Vol%).

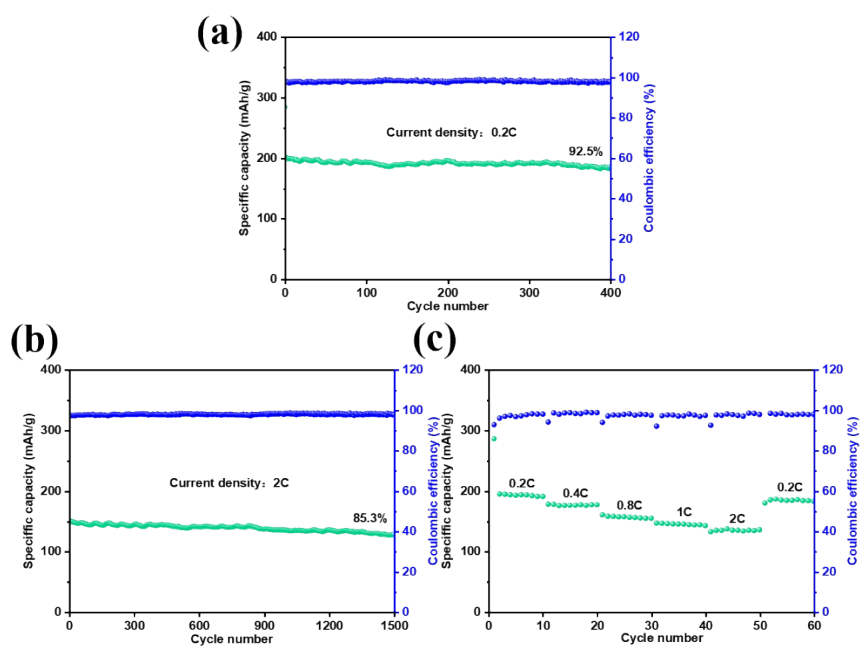


Figure S12. (a) Cycling performance and coulombic efficiency of the PT electrode at 0.2C. (b) Long-term cyclability of PT at a current density of 2.0C. (c) Rate performance of PT at different current densities from 0.2C to 2.0C.

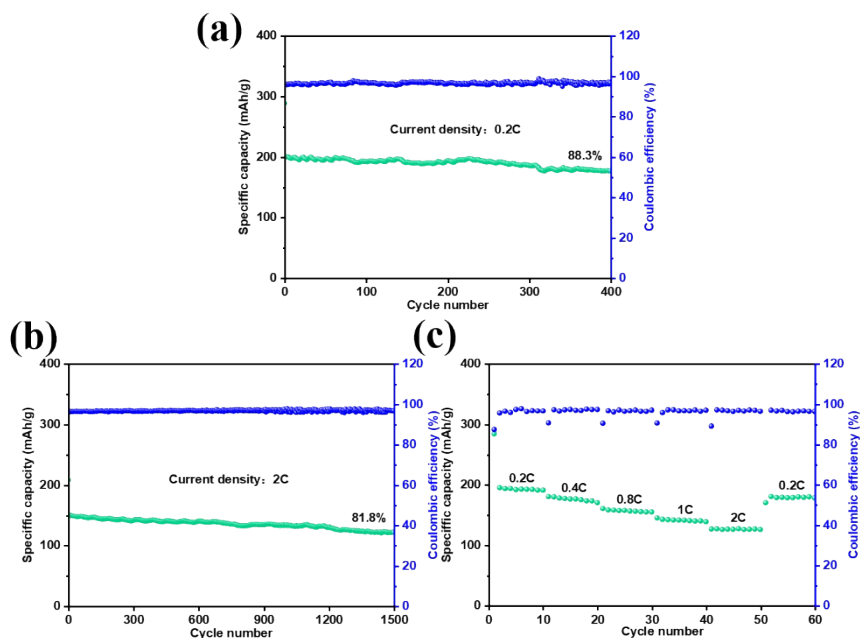


Figure S13. (a) Cycling performance and coulombic efficiency of the BP electrode at 0.2C. (b) Long-term cyclability of BP at a current density of 2.0C. (c) Rate performance of BP at different current densities from 0.2C to 2.0C.

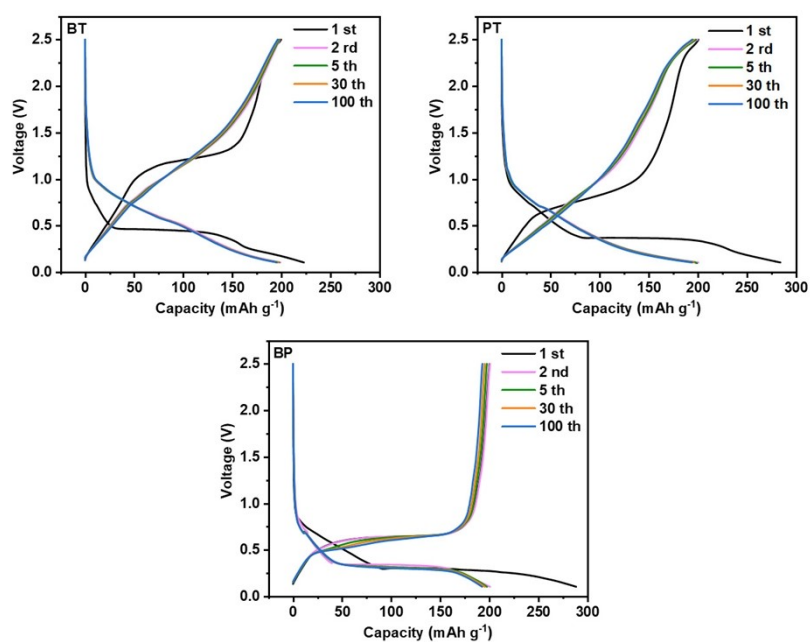


Figure S14. Galvanostatic discharge/charge profiles of (a) BT, (b) PT and (c) BP at a current density of 0.2C.

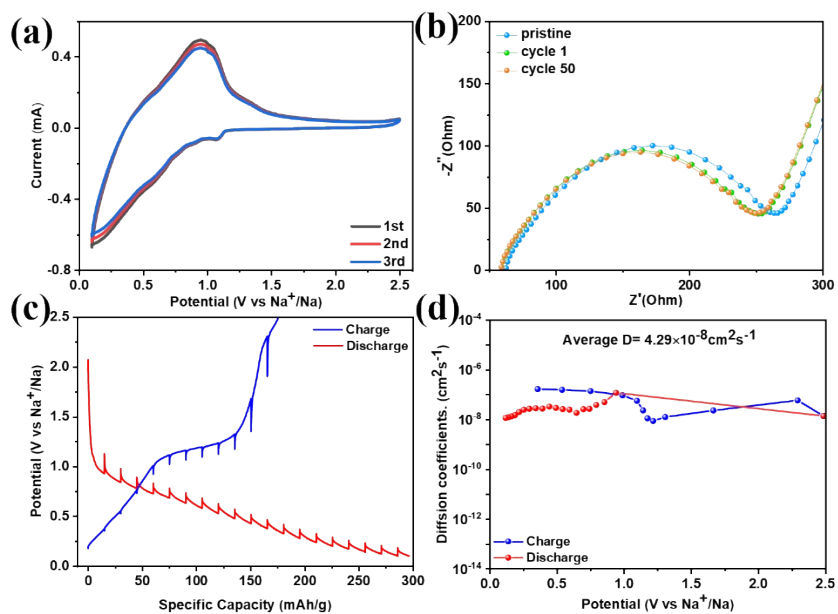


Figure S15. (a) CV curves of BT at 0.2 mV s^{-1} . (b) Nyquist plots of BT electrodes charged to 2.5 V after different cycles. (c) GITT curves and (d) the calculated Na-ion diffusion coefficients for BT electrode.

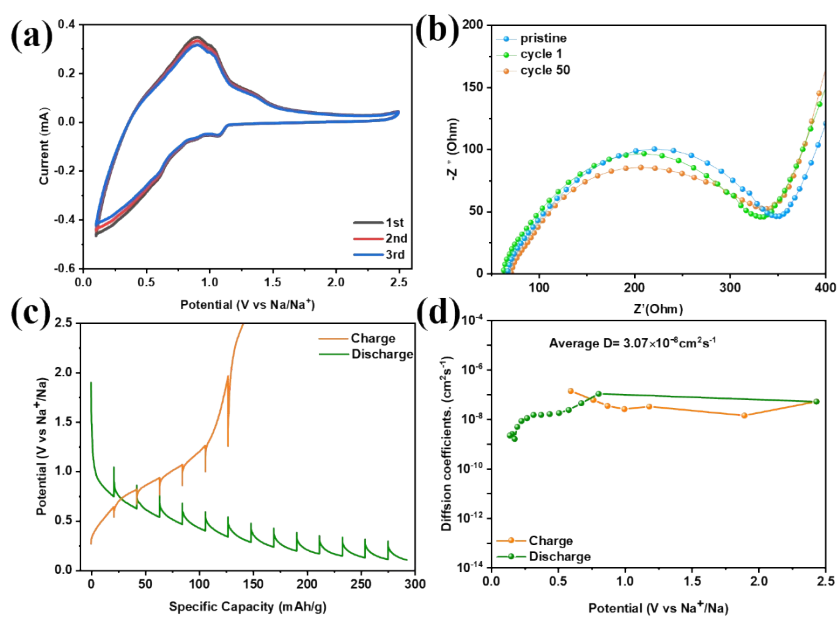


Figure S16. (a) CV curves of PT at 0.2 mV s^{-1} . (b) Nyquist plots of PT electrodes charged to 2.5 V after different cycles. (c) GITT curves and (d) the calculated Na-ion diffusion coefficients for PT electrode.

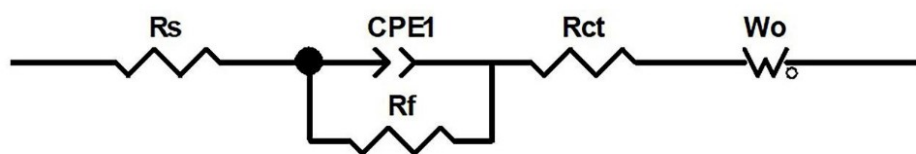


Figure S17. The equivalent circuits of EIS data for BT and PT in Na-ion batteries. R_s : electrolyte resistance, R_{ct} : charge transfer resistance, R_f : contact resistance of SEI films, CPE: constant phase element, and W_o : Warburg impedance. The simulated impedance parameters were determined by fitting the original EIS spectra using ZView software (inset).

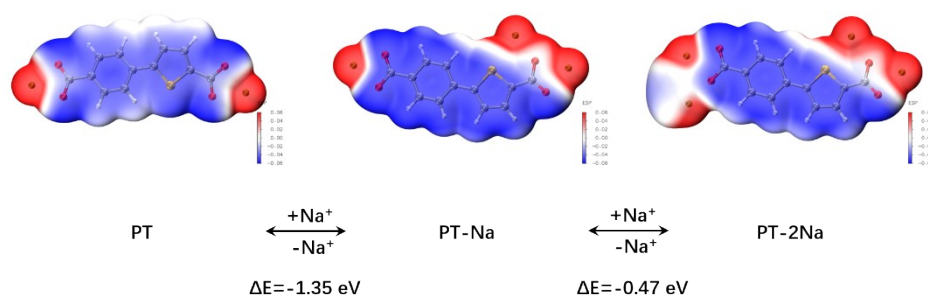


Figure S18. The calculated MESP distribution and the potential energy (ΔE) of PT with different numbers of Na^+ .

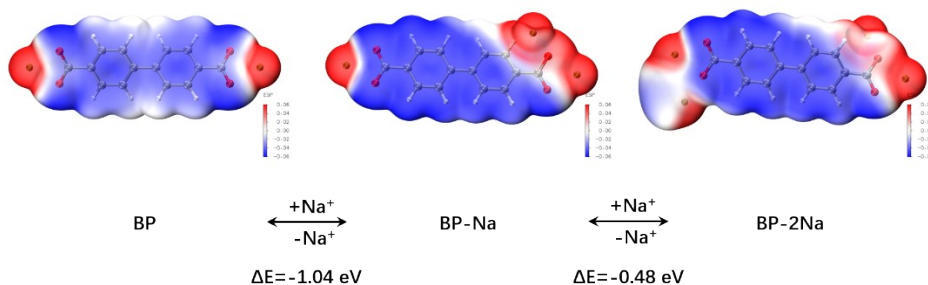


Figure S19. The calculated MESP distribution and the potential energy (ΔE) of BP with different numbers of Na^+ .

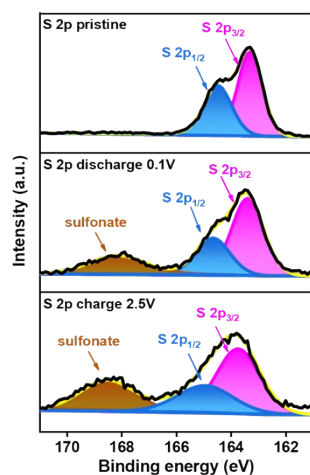


Figure S20. Ex-situ S 2p XPS spectra of the BT electrode in various states: pristine, discharged to 0.1 V and recharged to 2.5 V.

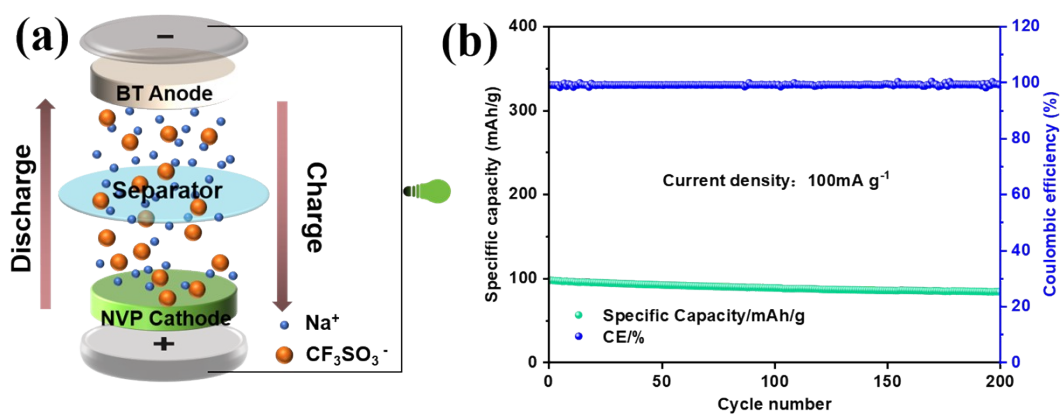


Figure S21. (a) Schematic diagram of the full battery during charging; (b) Cycle performance of full battery at 100 mA g^{-1} .

Table S1. Performances comparison between our anode and some reported organic anode materials for SIBs.

Materials	Current density (mA/g)	Cycle number	Specific capacity (mAh/g)	Capacity retention (%)	Ref
Na ₃ BTC	50	100	250	80	[1]
Na-DCA	50	200	124	51	[2]
Na ₂ NDC	40	70	209	70	[3]
Na ₂ TP	30	90	295	90	[4]
Na ₂ PDC	25.4	100	270	83	[5]
NS-Na ₂ TP	250	100	105	81	[6]
DFTP-Na	50	300	161	76	[7]
Na ₂ C ₈ H ₄ O ₄	25.5	50	225	74.4	[8]
Na ₄ C ₈ H ₂ O ₆	18.7	100	183	84	[9]
SSDC	50	50	222	90	[10]
Na ₂ TP@GE	100	500	207.9	77.3	[11]
BDTTS	50	100	230	91	[12]
S-PD	50	100	252	83	[13]
Na-CPP	100	300	197	99	[14]
Na ₄ C ₁₀ H ₂ O ₈	20	40	190	71	[15]
SCID	50	100	231	80	[16]
ADASS	34	100	170	92	[17]
BT	44.9	400	201	99	This work

Table S2. The thermal decomposition temperature comparison between our anode and some reported organic anode materials for SIBs.

Materials	Thermal decomposition temperature (°C)	Ref
Na ₃ BTC	500	[1]
Na ₂ NDC	550	[3]
Na ₂ PDC	523	[5]
Na ₂ TP@GE	500	[11]
ADASS	405	[17]
Na ₂ BDC	480	[18]
Na ₂ NC	400	[19]
Na-1, 2, 4-BTC	520	[20]
BT	548	This work

Table S3. Resistances of BT and PT in Na-ion batteries obtained from equivalent circuit fitting of impedance data.

cycle	BT		PT	
	R_s (Ω)	R_{ct} (Ω)	R_s (Ω)	R_{ct} (Ω)
Pristine	67.6	199.5	67.6	281.2
10	63.1	188.2	63.1	269
50	62.7	188.1	70.1	262.7

Table S4. Calculated LUMO and HOMO energies and distributions of BT, BT-Na and BT-2Na.

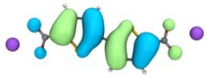
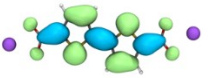
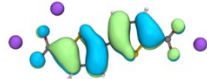
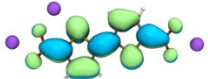
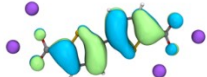
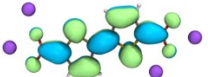
	HOMO	LUMO	GAP(eV)
BT	 -5.81	 -1.60	4.21
BT-Na	 -4.72	 -1.03	3.69
BT-2Na	 -4.83	 -1.16	3.67

Table S5. Calculated LUMO and HOMO energies and distributions of PT, PT-Na and PT-2Na.


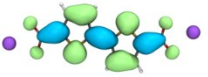
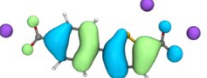
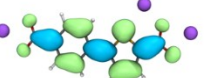
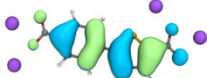
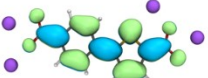
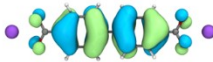
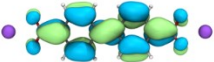
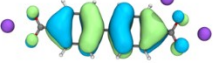
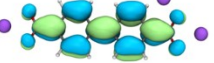
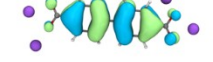
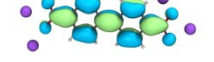
	HOMO	LUMO	GAP(eV)
PT	 -6.05	 -1.47	4.58
PT-Na	 -4.87	 -0.85	4.02
PT-2Na	 -5.00	 -1.06	3.94

Table S6. Calculated LUMO and HOMO energies and distributions of BP, BP -Na and BP -2Na.

	HOMO	LUMO	GAP(eV)
BP	 -6.40	 -1.25	5.15
BP-Na	 -5.18	 -0.80	4.38
BP-2Na	 -5.23	 -0.88	4.35

References

- [1] A. Tripathi, Y. Chen, H. Padhy, S. Manzhos, P. Balaya, *Energy Technology* **2019**,7, 1801030.
- [2] K. Holguin, K. Qin, E. P. Kamphaus, F. Chen, L. Cheng, G.-L. Xu, K. Amine, C. Luo, *J. Power Sources* **2022**, 533, 231383.
- [3] V. Medabalmi, N. Kuanr, K. Ramanujam, *Journal of The Electrochemical Society* **2018**, 165, A175.
- [4] Y. Park, D. S. Shin, S. H. Woo, N. S. Choi, K. H. Shin, S. M. Oh, K. T. Lee, S.Y. Hong, *Adv Mater.* **2012**, 24, 3562-3567.
- [5] H. Padhy, Y. Chen, J. Lüder, S. R. Gajella, S. Manzhos, P. Balaya, *Adv Energy Mater.* **2018**, 8, 1701572.
- [6] a) F. Wan, X.-L. Wu, J.-Z. Guo, J.-Y. Li, J.-P. Zhang, L. Niu, R.-S. Wang, *Nano Energy.* **2015**, 13, 450-457; b) R. R. Zhao, Y. L. Cao, X. P. Ai, H. X. Yang, *J Electroanal Chem.* **2013**, 688, 93-97.
- [7] J. Huang, K. I. E. Callender, K. Qin, M. Girgis, M. Paige, Z. Yang, A. Z. Clayborne, C. Luo, *ACS Appl. Mater. Interfaces* **2022**, 14, 40784–40792.
- [8] L. Zhao, J. Zhao, Y.-S. Hu, H. Li, Z. Zhou, M. Armand, L. Chen, *Adv Energy Mater.* **2012**, 2, 962-965.
- [9] S. Wang, L. Wang, Z. Zhu, Z. Hu, Q. Zhao, J. Chen, *Angew Chem Int Ed Engl.* **2014**, 53, 5892-5896.
- [10] C. Wang, Y. Xu, Y. Fang, M. Zhou, L. Liang, S. Singh, H. Zhao, A. Schober, Y. Lei, *J Am Chem Soc.* **2015**, 137, 3124-3130.
- [11] Y. Wang, K. Kretschmer, J. Zhang, A. K. Mondal, X. Guo, G. Wang, *Rsc Adv.* **2016**, 6, 57098-57102.
- [12] Y. Luo, K. Jia, X. Li, J. Zhang, G. Huang, C. Zhong, L. Zhu, F. Wu, *ChemSusChem* **2024**, e202301847.
- [13] K. Jia, L. Zhu, F. Wu, *ChemSusChem* **2021**, 14, 3124–3130.
- [14] K. Jia, H. Liu, G. Huang, J. Zhang, X. Liu, L. Li, L. Zhu, F. Wu, *J. Mater. Chem. A* **2022**, 10, 14917–14922.

- [15] K. Qin, K. Holguin, M. Mohammadiroudbari, C. Luo, Chem. Commun. **2021**, 57, 2360–2363.
- [16] L.-Y. Wang, C. Ma, X. Wei, B. Chang, K.-X. Wang, J.-S. Chen, J. Mater. Chem. A **2020**, 8, 8469–8475.
- [17] C. Luo, G.-L. Xu, X. Ji, S. Hou, L. Chen, F. Wang, J. Jiang, Z. Chen, Y. Ren, K. Amine, C. Wang, Angew. Chem. Int. Edit. **2018**, 57, 2879–2883.
- [18] A. Abouimrane, W. Weng, H. Eltayeb, Y. Cui, J. Niklas, O. Poluektov, K. Amine, Energy & Environmental Science. **2012**, 5, 9632-9638.
- [19] W. Deng, J. Qian, Y. Cao, X. Ai, H. Yang, Small. **2016**, 12, 583-587.
- [20] T. Gu, S. Gao, J. Wang, S. Cao, K. Wang, M. Zhou, K. Jiang, ChemElectroChem **2020**, 7, 3517.